

Multiple-GPU accelerated high-order gas-kinetic scheme on three-dimensional unstructured meshes

Yuhang Wang^a, Waixiang Cao^a, Liang Pan^{a,*}

^aLaboratory of Mathematics and Complex Systems, School of Mathematical Sciences, Beijing Normal University, Beijing, China

Abstract

Recently, successes have been achieved for the high-order gas-kinetic schemes (HGKS) on unstructured meshes for compressible flows. In this paper, to accelerate the computation, HGKS is implemented with the graphical processing unit (GPU) using the compute unified device architecture (CUDA). HGKS on unstructured meshes is a fully explicit scheme, and the acceleration framework can be developed based on the cell-level parallelism. For single-GPU computation, the connectivity of geometric information is generated for the requirement of data localization and independence. Based on such data structure, the kernels and corresponding grids of CUDA are set. With the one-to-one mapping between the indices of cells and CUDA threads, the single-GPU computation using CUDA can be implemented for HGKS. For multiple-GPU computation, the domain decomposition and data exchange need to be taken into account. The domain is decomposed into subdomains by METIS, and the MPI processes are created for the control of each process and communication among GPUs. With reconstruction of connectivity and adding ghost cells, the main configuration of CUDA for single-GPU can be inherited by each GPU. The benchmark cases for compressible flows, including accuracy test and flow passing through a sphere, are presented to assess the numerical performance of HGKS with Nvidia RTX A5000 and Tesla V100 GPUs. For single-GPU computation, compared with the parallel central processing unit (CPU) code running on the Intel Xeon Gold 5120 CPU with open multi-processing (OpenMP) directives, 5x speedup is achieved by RTX A5000 and 9x speedup is achieved by Tesla V100. For multiple-GPU computation, HGKS code scales properly with the increasing number of GPU. Numerical results confirm the excellent performance of multiple-GPU accelerated HGKS on unstructured meshes.

Keywords: High-order gas-kinetic scheme, unstructured meshes, WENO reconstruction, GPU accelerated computation.

*Corresponding author

Email addresses: hskwyh@outlook.com (Yuhang Wang), caowx@bnu.edu.cn (Waixiang Cao), panliang@bnu.edu.cn (Liang Pan)

1. Introduction

Graphical processing unit (GPU) is a form of hardware acceleration, which is originally developed for graphics manipulation and is extremely efficient at processing large amounts of data in parallel. Since these units have a parallel computation capability inherently, they can provide fast and low cost solutions to high performance computing (HPC). In recent years, GPUs have gained significant popularity as a cheaper, more efficient, and more accessible alternative to large-scale HPC systems with central processing units (CPU). Great effort has been already achieved for computational fluid dynamics, such as direct numerical simulation of turbulent flows [5, 29, 20], high-order CFD simulations with complex grids [20], incompressible smoothed particle hydrodynamics [24], multiphase flows [7], shallow water flows [6], unified gas kinetic wave-particle method [8] and discrete unified gas kinetic scheme [13], etc.

In the past decades, the gas-kinetic scheme (GKS) has been developed systematically based on the Bhatnagar-Gross-Krook (BGK) model [1, 3] under the finite volume framework, and applied successfully in the computations from low speed flow to hypersonic one [25, 26]. The gas-kinetic scheme presents a gas evolution process from kinetic scale to hydrodynamic scale, where both inviscid and viscous fluxes are recovered from a time-dependent and genuinely multi-dimensional gas distribution function at a cell interface. Starting from a time-dependent flux function, based on the two-stage fourth-order formulation [16, 17], the high-order gas-kinetic scheme (HGKS) has been constructed and applied for the compressible flow simulation [19, 11, 27]. Originally, the parallel HGKS code was developed with central processing unit (CPU) using open multi-processing (OpenMP) directives. However, due to the limited shared memory, the computational scale is constrained. To perform the large-scale numerical simulation of turbulence, the domain decomposition and the message passing interface (MPI) [9] are used for parallel implementation [2]. To further improve the efficiency, the HGKS code is implemented with single GPU. A major limitation in single-GPU computation is its available memory, which leads to a bottleneck in the maximum number of computational mesh. To implement much larger scale computation and accelerate the efficiency, HGKS is implemented with multiple GPUs using CUDA and MPI architecture (MPI + CUDA). Due to the explicit formulation of HGKS, the CPU code with MPI scales properly with the number of processors used. The numerical results demonstrates the capability of HGKS as a powerful DNS tool from the low speed to supersonic turbulence study [2]. Recently, the three-dimension discontinuous Galerkin based HGKS has been implemented in single-GPU computation using compute unified device architecture (CUDA) [22, 23]. Obtained results are compared with those obtained by Intel i7-9700 CPU using OpenMP directives. The GPU code achieves 6x-7x speedup with TITAN RTX, and 10x-11x speedup with Tesla V100. The computational time of parallel CPU code running on 1024 Intel Xeon E5-2692 cores with MPI is approximately 3 times longer than that of GPU code using 8 Tesla V100 GPUs with MPI and CUDA.

To deal with the complicated geometry, the high-order gas-kinetic scheme on unstructured meshes has been developed with the WENO reconstruction [27, 28]. Due to the complex mesh topology of hybrid unstructured meshes, the procedures of classical WENO

scheme, including the selection of candidate stencils and calculation of linear weights, become extremely complicated. A simple strategy of selecting stencils for reconstruction is adopted and the topology independent linear weights are used. A large stencil is selected with the neighboring cells and the neighboring cells of neighboring cells, and a quadratic polynomial can be obtained. A robust selections of candidate sub-stencils are also given, such that the linear polynomials are solvable for each sub-stencil. In this paper, to accelerate the computation, HGKS on unstructured meshes is implemented with GPU using CUDA. The current HGKS is a fully explicit scheme, and the acceleration of computation can be achieved by executing the calculation of the cells simultaneously. Compared with the structured meshes, the connectivity of geometric information for unstructured meshes needs to be generated for the requirement of data localization and independence. Based on such data structure, the kernels and corresponding grids of CUDA are set. With the one-to-one mapping between the indices of cells and CUDA threads, the single-GPU computation using CUDA can be implemented for HGKS. For multiple-GPU computation, the domain decomposition and data exchange, which are more complicated than that of structured meshes, need to be taken into account. The domain is decomposed into several subdomains by METIS [12], and the MPI processes are created for one-to-one GPU management and communication. The CUDA-Aware MPI library [14] is used for GPU-GPU communication. With reconstruction of connectivity and adding three-layer of ghost cells, the main configuration of CUDA for single-GPU can be inherited by each GPU. The mappings between two subdomains are built for the transfer of conservative variables of ghost cells. Non-blocking communication and the corresponding strategy are used to improve the efficiency of GPU-GPU communication. For single-GPU implementation using CUDA, compared with the CPU code using 2 Intel(R) Xeon(R) Gold 5120 CPUs with OpenMP directives, 5x speedup is achieved for RTX A5000 and 9x speedup is achieved for Tesla V100. For multiple-GPU with CUDA and MPI, the HGKS is strongly scalable with the increasing number of GPUs. Nearly linear speedup can be achieved under suitable computational work-load. Numerical performance shows that the data communication crossing GPUs through MPI costs the relative little time. To reduce the memory cost and improve the computational efficiency, the code of multiple-GPU accelerated HGKS is compiled using FP32 (single) precision for the accuracy test. As expected, the efficiency can be improved and the memory cost can be reduced with FP32 precision. Compared with the results of FP64 (double) precision, the errors of the accuracy increase slightly and the third-order can be maintained.

This paper is organized as follows. In Section 2, the high-order gas-kinetic scheme is briefly reviewed. The single-GPU implementation for HGKS code is introduced in Section 3. Section 4 includes the multiple-GPU implementation. The numerical results are presented in Section 5. The last section is the conclusion.

2. High-order gas-kinetic scheme

2.1. BGK equation and finite volume scheme

The Boltzmann equation expresses the behavior of a many-particle kinetic system in terms of the evolution equation for a single particle gas distribution function. The BGK

equation [1, 3] is the simplification of Boltzmann equation, and the three-dimensional BGK equation can be written as

$$f_t + uf_x + vf_y + wf_z = \frac{g - f}{\tau}, \quad (1)$$

where $\mathbf{u} = (u, v, w)$ is the particle velocity, τ is the collision time, f is the gas distribution function. g is the equilibrium state given by Maxwellian distribution

$$g = \rho \left(\frac{\lambda}{\pi}\right)^{(N+3)/2} e^{-\lambda[(u-U)^2 + (v-V)^2 + (w-W)^2 + \xi^2]},$$

where ρ is the density, $\mathbf{U} = (U, V, W)$ is the macroscopic fluid velocity, and λ is the inverse of gas temperature, i.e., $\lambda = m/2kT$. In the BGK model, the collision operator involves a simple relaxation from f to the local equilibrium state g . The variable ξ accounts for the internal degree of freedom, $\xi^2 = \xi_1^2 + \dots + \xi_N^2$, $N = (5 - 3\gamma)/(\gamma - 1)$ is the internal degree of freedom, and γ is the specific heat ratio. The collision term satisfies the compatibility condition

$$\int \frac{g - f}{\tau} \psi d\Xi = 0,$$

where $\psi = (1, u, v, w, \frac{1}{2}(u^2 + v^2 + w^2 + \xi^2))^T$ and $d\Xi = dudvdwd\xi_1 \dots d\xi_N$. According to the Chapman-Enskog expansion for BGK equation, the macroscopic governing equations can be derived. In the continuum region, the BGK equation can be rearranged and the gas distribution function can be expanded as

$$f = g - \tau D_{\mathbf{u}} g + \tau D_{\mathbf{u}} (\tau D_{\mathbf{u}}) g - \tau D_{\mathbf{u}} [\tau D_{\mathbf{u}} (\tau D_{\mathbf{u}}) g] + \dots,$$

where $D_{\mathbf{u}} = \frac{\partial}{\partial t} + \mathbf{u} \cdot \nabla$. With the zeroth-order truncation $f = g$, the Euler equations can be obtained. For the first-order truncation

$$f = g - \tau(ug_x + vg_y + wg_z + g_t),$$

the Navier-Stokes equations can be obtained [25, 26].

Taking moments of Eq.(1) and integrating with respect to space, the semi-discretized finite volume scheme can be expressed as

$$\frac{dQ_i}{dt} = \mathcal{L}(Q_i), \quad (2)$$

where $Q_i = (\rho, \rho U, \rho V, \rho W, \rho E)$ is the cell averaged conservative value of Ω_i , ρ is the density, U, V, W is the flow velocity and ρE is the total energy density. The operator \mathcal{L} is defined as

$$\mathcal{L}(Q_i) = -\frac{1}{|\Omega_i|} \sum_{i_p \in N(i)} F_{i,i_p}(t) S_{i_p} = -\frac{1}{|\Omega_i|} \sum_{i_p \in N(i)} \iint_{\Sigma_{i_p}} \mathbf{F}(Q, t) d\sigma, \quad (3)$$

where $|\Omega_i|$ is the volume of Ω_i , Σ_{i_p} is the common cell interface of Ω_i , S_{i_p} is the area of Σ_{i_p} and $N(i)$ is the set of index for neighboring cells of Ω_i . To achieve the expected order of accuracy, the Gaussian quadrature is used for the flux integration

$$\iint_{\Sigma_{i_p}} \mathbf{F}(Q, t) d\sigma = \sum_G \omega_G F_G(t) S_{i_p},$$

where ω_G is the quadrature weights. The numerical flux $F_G(t)$ at Gaussian quadrature point \mathbf{x}_G can be given by taking moments of gas distribution function

$$F_G(t) = \int \boldsymbol{\psi} \mathbf{u} \cdot \mathbf{n}_G f(\mathbf{x}_G, t, \mathbf{u}, \xi) d\Xi, \quad (4)$$

where $F_G(t) = (F_G^\rho, F_G^{\rho U}, F_G^{\rho V}, F_G^{\rho W}, F_G^{\rho E})$ and \mathbf{n}_G is the local normal direction of cell interface. With the coordinate transformation, the numerical flux in the global coordinate can be obtained. Based on the integral solution of BGK equation Eq.(1), the gas distribution function $f(\mathbf{x}_G, t, \mathbf{u}, \xi)$ in the local coordinate can be given by

$$f(\mathbf{x}_G, t, \mathbf{u}, \xi) = \frac{1}{\tau} \int_0^t g(\mathbf{x}', t', \mathbf{u}, \xi) e^{-(t-t')/\tau} dt' + e^{-t/\tau} f_0(-\mathbf{u}t, \xi),$$

where $\mathbf{x}' = \mathbf{x}_G - \mathbf{u}(t - t')$ is the trajectory of particles, f_0 is the initial gas distribution function, and g is the corresponding equilibrium state. With the first order spatial derivatives, the second-order gas distribution function at cell interface can be expressed as

$$\begin{aligned} f(\mathbf{x}_G, t, \mathbf{u}, \xi) = & (1 - e^{-t/\tau})g_0 + ((t + \tau)e^{-t/\tau} - \tau)(\bar{a}_1 u + \bar{a}_2 v + \bar{a}_3 w)g_0 \\ & + (t - \tau + \tau e^{-t/\tau})\bar{A}g_0 \\ & + e^{-t/\tau}g_r[1 - (\tau + t)(a_1^r u + a_2^r v + a_3^r w) - \tau A^r](1 - H(u)) \\ & + e^{-t/\tau}g_l[1 - (\tau + t)(a_1^l u + a_2^l v + a_3^l w) - \tau A^l]H(u), \end{aligned} \quad (5)$$

where the equilibrium state g_0 and the corresponding conservative variables Q_0 can be determined by the compatibility condition

$$\int \boldsymbol{\psi} g_0 d\Xi = Q_0 = \int_{u>0} \boldsymbol{\psi} g_l d\Xi + \int_{u<0} \boldsymbol{\psi} g_r d\Xi.$$

With the reconstruction of macroscopic variables, the coefficients in Eq.(5) can be fully determined by the reconstructed derivatives and compatibility condition

$$\begin{aligned} \langle a_1^k \rangle &= \frac{\partial Q_k}{\partial \mathbf{n}_x}, \langle a_2^k \rangle = \frac{\partial Q_k}{\partial \mathbf{n}_y}, \langle a_3^k \rangle = \frac{\partial Q_k}{\partial \mathbf{n}_z}, \langle a_1^k u + a_2^k v + a_3^k w + A^k \rangle = 0, \\ \langle \bar{a}_1 \rangle &= \frac{\partial Q_0}{\partial \mathbf{n}_x}, \langle \bar{a}_2 \rangle = \frac{\partial Q_0}{\partial \mathbf{n}_y}, \langle \bar{a}_3 \rangle = \frac{\partial Q_0}{\partial \mathbf{n}_z}, \langle \bar{a}_1 u + \bar{a}_2 v + \bar{a}_3 w + \bar{A} \rangle = 0, \end{aligned}$$

where $k = l$ and r , \mathbf{n}_x , \mathbf{n}_y , \mathbf{n}_z are the unit directions of local coordinate at \mathbf{x}_G and $\langle \dots \rangle$ are the moments of the equilibrium g and defined by

$$\langle \dots \rangle = \int g(\dots) \psi d\Xi.$$

More details of the gas-kinetic scheme can be found in [25, 26].

2.2. Temporal reconstruction

In this paper, the two-stage fourth-order temporal discretization [16, 19] is used to achieve the high-order temporal accuracy. For the semi-discretized finite volume scheme Eq.(2), the flow variables Q^{n+1} at $t_{n+1} = t_n + \Delta t$ can be updated with the following formula

$$\begin{aligned} Q_i^* &= Q_i^n + \frac{1}{2}\Delta t \mathcal{L}(Q_i^n) + \frac{1}{8}\Delta t^2 \frac{\partial}{\partial t} \mathcal{L}(Q_i^n), \\ Q_i^{n+1} &= Q_i^n + \Delta t \mathcal{L}(Q_i^n) + \frac{1}{6}\Delta t^2 \left(\frac{\partial}{\partial t} \mathcal{L}(Q_i^n) + 2 \frac{\partial}{\partial t} \mathcal{L}(Q_i^*) \right). \end{aligned}$$

It can be proved that the above temporal discretization provides a fourth-order time accurate solution for hyperbolic equations [16]. To implement the two-stage method for Eq.(2), a linear function is used to approximate the time dependent numerical fluxes Eq.(4)

$$F_G(t) = F_G^n + \partial_t F_G^n (t - t_n). \quad (6)$$

Integrating Eq.(6) over $[t_n, t_n + \Delta t/2]$ and $[t_n, t_n + \Delta t]$, we have the following two equations

$$\begin{aligned} F_G^n \Delta t + \frac{1}{2} \partial_t F_G^n \Delta t^2 &= \int_{t_n}^{t_n + \Delta t} F_G(t) dt, \\ \frac{1}{2} F_G^n \Delta t + \frac{1}{8} \partial_t F_G^n \Delta t^2 &= \int_{t_n}^{t_n + \Delta t/2} F_G(t) dt. \end{aligned}$$

The coefficients F_G^n and $\partial_t F_G^n$ can be determined by solving the linear system above, and the operator \mathcal{L} and its temporal derivative $\partial_t \mathcal{L}$ at $t = t_n$ can be given according to Eq.(3). Similarly, \mathcal{L} and $\partial_t \mathcal{L}$ at the intermediate state $t = t_n + \Delta t/2$ can be constructed as well.

2.3. Spatial reconstruction

To deal with the complex geometry, the three-dimensional unstructured meshes are considered, and the tetrahedral and hexahedral meshes are used in this paper for simplicity. In the previous studies, the high-order gas-kinetic schemes have been developed with the third-order non-compact WENO reconstruction [27, 28, 30, 31]. In this section, a brief review of WENO reconstruction on unstructured hexahedral and tetrahedral meshes will be presented.

For the cell Ω_i , the faces are labeled as f_p , where $p = 1, \dots, 4$ for tetrahedral cell, and $p = 1, \dots, 6$ for hexahedral cell. The neighboring cell of Ω_i , which shares the face f_p , is

denoted as Ω_{i_p} . Meanwhile, the neighboring cells of Ω_{i_p} are denoted as $\Omega_{i_{pm}}$. For WENO reconstruction, a big stencil for cell Ω_i is selected as follows

$$S_i^{WENO} = \{\Omega_i, \Omega_{i_p}, \Omega_{i_{pm}}\},$$

which is consist of neighboring cells and neighboring cells of neighboring cells of Ω_i . To deal with the discontinuity, the sub-stencils S_m^{WENO} in non-compact WENO reconstruction for cell Ω_i are selected, where $m = 1, \dots, M$ and M is the number of sub-stencils. For the hexahedral cell, $M = 8$ and the sub-candidate stencils are selected as

$$\begin{aligned} S_{i_1}^{WENO} &= \{\Omega_i, \Omega_{i_1}, \Omega_{i_2}, \Omega_{i_3}\}, & S_{i_5}^{WENO} &= \{\Omega_i, \Omega_{i_6}, \Omega_{i_2}, \Omega_{i_3}\}, \\ S_{i_2}^{WENO} &= \{\Omega_i, \Omega_{i_1}, \Omega_{i_3}, \Omega_{i_4}\}, & S_{i_6}^{WENO} &= \{\Omega_i, \Omega_{i_6}, \Omega_{i_3}, \Omega_{i_4}\}, \\ S_{i_3}^{WENO} &= \{\Omega_i, \Omega_{i_1}, \Omega_{i_4}, \Omega_{i_5}\}, & S_{i_7}^{WENO} &= \{\Omega_i, \Omega_{i_6}, \Omega_{i_4}, \Omega_{i_5}\}, \\ S_{i_4}^{WENO} &= \{\Omega_i, \Omega_{i_1}, \Omega_{i_5}, \Omega_{i_2}\}, & S_{i_8}^{WENO} &= \{\Omega_i, \Omega_{i_6}, \Omega_{i_5}, \Omega_{i_2}\}. \end{aligned}$$

The linear polynomials can be determined based on above stencils, which contain the target cell Ω_i and three neighboring cells. For the tetrahedral cells, in order to avoid the centroids of Ω_i and three of neighboring cells becoming coplanar, additional cells are needed for the sub-candidate stencils. For the tetrahedral cell, four sub-candidate stencils are selected as

$$\begin{aligned} S_{i_1}^{WENO} &= \{\Omega_i, \Omega_{i_1}, \Omega_{i_2}, \Omega_{i_3}, \Omega_{i_{11}}, \Omega_{i_{12}}, \Omega_{i_{13}}\}, \\ S_{i_2}^{WENO} &= \{\Omega_i, \Omega_{i_1}, \Omega_{i_2}, \Omega_{i_4}, \Omega_{i_{21}}, \Omega_{i_{22}}, \Omega_{i_{23}}\}, \\ S_{i_3}^{WENO} &= \{\Omega_i, \Omega_{i_2}, \Omega_{i_3}, \Omega_{i_4}, \Omega_{i_{31}}, \Omega_{i_{32}}, \Omega_{i_{33}}\}, \\ S_{i_4}^{WENO} &= \{\Omega_i, \Omega_{i_3}, \Omega_{i_1}, \Omega_{i_4}, \Omega_{i_{41}}, \Omega_{i_{42}}, \Omega_{i_{43}}\}. \end{aligned}$$

The cells of sub-candidate stencils are consist of the three neighboring cells and three neighboring cells of one neighboring cell. With such an enlarged sub-stencils, the linear polynomials can be determined.

With the selected stencil, a quadratic polynomial and several linear polynomials can be constructed based on the big stencil and the sub-stencils as follows

$$\begin{aligned} P_0(\mathbf{x}) &= Q_0 + \sum_{|\mathbf{d}|=1}^2 a_{\mathbf{d}} p_{\mathbf{d}}(\mathbf{x}), \\ P_m(\mathbf{x}) &= Q_0 + \sum_{|\mathbf{d}|=1} b_{\mathbf{d}}^m p_{\mathbf{d}}(\mathbf{x}), \end{aligned} \tag{7}$$

where $m = 1, \dots, M$, Q_0 is the cell averaged variables over Ω_0 with newly rearranged index, the multi-index $\mathbf{d} = (d_1, d_2, d_3)$ and $|\mathbf{d}| = d_1 + d_2 + d_3$. The base function $p_{\mathbf{d}}(\mathbf{x})$ is defined as

$$p_{\mathbf{d}}(\mathbf{x}) = x^{d_1} y^{d_2} z^{d_3} - \frac{1}{|\Omega_0|} \iiint_{\Omega_0} x^{d_1} y^{d_2} z^{d_3} dV.$$

To determine these polynomials for WENO reconstruction, the following constraints need to be satisfied

$$\begin{aligned}\frac{1}{|\Omega_k|} \iiint_{\Omega_k} P_0(\mathbf{x}) dV &= Q_k, \quad \Omega_k \in S_i^{WENO}, \\ \frac{1}{|\Omega_{m_k}|} \iiint_{\Omega_k} P_m(\mathbf{x}) dV &= Q_k, \quad \Omega_k \in S_{i_m}^{WENO},\end{aligned}$$

where $k = 0, \dots, K$, $m_k = 0, \dots, m_K$, Q_k and Q_{m_k} are the conservative variable with newly rearranged index. The over-determined linear systems can be generated and the least square method is used to obtain the coefficients a_d and b_d^m .

With the reconstructed polynomial $P_m(\mathbf{x})$, $m = 0, \dots, M$, the point-value $Q(\mathbf{x}_G)$ and the spatial derivatives $\partial_{x,y,z} Q(\mathbf{x}_G)$ for reconstructed variables at Gaussian quadrature point can be given by the non-linear combination

$$\begin{aligned}Q(\mathbf{x}_G) &= \bar{\omega}_0 \left(\frac{1}{\gamma_0} P_0(\mathbf{x}_G) - \sum_{m=1}^M \frac{\gamma_m}{\gamma_0} P_m(\mathbf{x}_G) \right) + \sum_{m=1}^M \bar{\omega}_m P_m(\mathbf{x}_G), \\ \partial_{x,y,z} Q(\mathbf{x}_G) &= \bar{\omega}_0 \left(\frac{1}{\gamma_0} \partial_{x,y,z} P_0(\mathbf{x}_G) - \sum_{m=1}^M \frac{\gamma_m}{\gamma_0} \partial_{x,y,z} P_m(\mathbf{x}_G) \right) + \sum_{m=1}^M \bar{\omega}_m \partial_{x,y,z} P_m(\mathbf{x}_G),\end{aligned}\tag{8}$$

where $\gamma_0, \gamma_1, \dots, \gamma_M$ are the linear weights. The non-linear weights ω_m and normalized non-linear weights $\bar{\omega}_m$ are defined as

$$\bar{\omega}_m = \frac{\omega_m}{\sum_{m=0}^M \omega_m}, \quad \omega_m = \gamma_m \left[1 + \left(\frac{\tau_Z}{\beta_m + \epsilon} \right) \right], \quad \tau_Z = \sum_{m=1}^M \left(\frac{|\beta_0 - \beta_m|}{M} \right),$$

where ϵ is a small positive number. The smooth indicator β_m is defined as

$$\beta_m = \sum_{|l|=1}^{r_m} |\Omega_i|^{\frac{2|l|}{3}-1} \int_{\Omega_i} \left(\frac{\partial^l P_m}{\partial x^{l_1} \partial y^{l_2} \partial z^{l_3}}(x, y, z) \right)^2 dV,$$

where $r_0 = 2$ and $r_m = 1$ for $m = 1, \dots, M$. It can be proved that Eq.(8) ensures third-order accuracy and more details can be found in [27, 28]. In the computation, the linear weights are set as $\gamma_i = 0.025$, $\gamma_0 = 1 - \gamma_i M$ for both non-compact and compact scheme without special statement.

3. Single-GPU implementation

With the development of hardware and software, GPUs are becoming an important part of high performance computing, which provide great computational power for large-scale scientific problem. In the previous studies [22, 23], the parallel acceleration for HGKS on structured meshes is implemented by GPUs with Compute Unified Device Architecture

(CUDA) and Message Passing Interface (MPI). The multiple-GPU accelerated HGKS code scales properly with the increasing number of GPU. In this paper, the multiple-GPU accelerated HGKS code will be extended to unstructured meshes. HGKS on unstructured meshes is a fully explicit scheme, and the idea of parallelism at the cell level is retained, which means that the acceleration can be achieved by performing calculations on a large number of cells simultaneously. In this section, we mainly focus on the single-GPU implementation with CUDA. The multiple-GPU implementation with MPI and CUDA will be presented in next section.

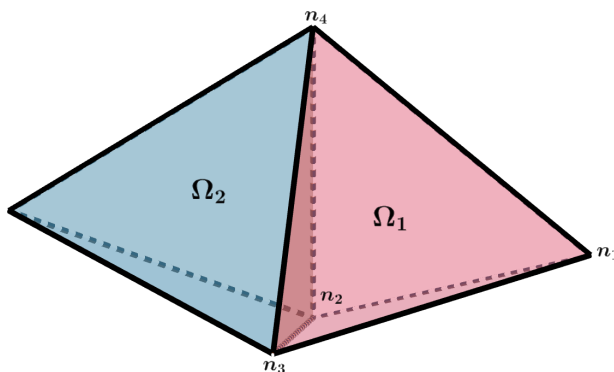


Figure 1: Data structure of unstructured meshes in HGKS.

3.1. Generation of geometric information

For the structured meshes, the computational domain is consist of cells, which are distinguished by the indices (i, j, k) . These indices are directly connected with the way of storage for flow field and geometric data in the computer. The topological relationships for computational mesh (node, face and cell) can be obtained naturally. Thus, the data localization and independence are easily achieved. However, it is not natural for the unstructured meshes, in which all geometric information is stored in one-dimensional arrays. Each cell, face, node owns a unique index, and the adjacent indices cannot be provided directly. Therefore, the additional geometric connectivities need to be built for the cell-level parallelization of HGKS.

Three main parts of algorithm are taken into consideration: WENO reconstruction, GKS flux solver, temporal discretization. To update the conservative variables of a control volume, the numerical fluxes and its temporal derivatives at the cell interfaces need be provided. To calculate the fluxes and its temporal derivatives, the conservative variables of two-layer neighbors should be accessed for WENO reconstruction. Besides, the node coordinates for each cell are needed for the generation of geometric information, such as the area, volume and local coordinate systems. Thus, the cell-to-node, face-to-node, cell-to-face, face-to-cell, and cell-to-neighbor connectivities need to be constructed. As shown in Figure.1, the tetrahedral cell is taken as an example, and these geometric connectivities can be built as follows

1. Cell-to-node and face-to-node connectivities can be provided by two two-dimensional arrays, i.e., *FaceNode* and *CellNode*, respectively. As shown in Figure.1, there are four nodes for cell Ω_1 , i.e., n_1, n_2, n_3, n_4 , and four faces, i.e., $f_1 = \{n_2, n_3, n_4\}, f_2 = \{n_1, n_3, n_4\}, f_3 = \{n_1, n_2, n_4\}, f_4 = \{n_1, n_2, n_3\}$. Therefore, the connectivities are described by $CellNode[\Omega_1][4] = \{n_1, n_2, n_3, n_4\}$ and $FaceNode[f_1][3] = \{n_2, n_3, n_4\}$, where the second index of two arrays should be changes according to the type of cell.
2. Cell-to-face and face-to-cell connectivities is defined by two two-dimensional arrays, i.e., *CellFace* and *FaceCell*. As shown in Figure.1, the cell Ω_1 is composed by four faces (f_1, f_2, f_3, f_4) and the cell Ω_1 and Ω_2 share the common face f_1 . The connectivity is described by $CellFace[\Omega_1][4] = \{f_1, f_2, f_3, f_4\}$ and $FaceNeighbor[f_1][2] = \{\Omega_1, \Omega_2\}$. The second index of *CellFace* varies according to the type of cell. For the boundary face f^* , $FaceNeighbor[f^*][2] = \{\Omega_*, 0\}$, where 0 is a label for boundary cell.
3. Cell-to-neighbor connectivity can be also defined by a two-dimensional array, i.e., *CellNeighbor*. Compared with the connectivities above, it can be built by a traversal search with the cell-to-face and face-to-cell connectivities. *CellFace* provides the index of faces belonging to each cell, and the neighbors can be obtained by traverse corresponding *FaceCell*. According to the data stored in *FaceCell*, 0 will be received for the boundary cell and it will be replaced by the cell rank obtained by using boundary condition. With the procedure above, the cell-to-neighbor connectivity is obtained by $CellNeighbor[\Omega][\Omega_1, \Omega_2, \dots, \Omega_n]$, where n varies according to the type of meshes.
4. With the cell-to-neighbor connectivity of neighboring cells of Ω , the collection of two-layer neighbors of Ω can be obtained. Based on the collection of two-layer neighbors, HGKS on unstructured meshes can be implemented with WENO reconstruction. The process of building such connectivities is shown in Algorithm.1.

Algorithm 1 Build relationship between two-layer neighbors and cells

```

for CellRank = 1 to NumTotalCell do
  for FirstLayerCellRank = 1 to NumTotalCellNeighbor do
    FNeighborID  $\leftarrow$  CellNeighbor[CellRank][FirstLayerCellRank]
    for SecondLayerCellRank = 1 to NumTotalFirstNeighbor do
      SNeighborID  $\leftarrow$  CellNeighbor[FNeighborID][SecondLayerCellRank]
      if SNeighborID == 0 then
        Add ghost cell according to boundary condition
      end if
      if SNeighborID does not exist in CellNeighbor[CellRank][*] then
        Add SNeighborID  $\rightarrow$  CellNeighbor[CellRank][*]
      end if
    end for
  end for
end for

```

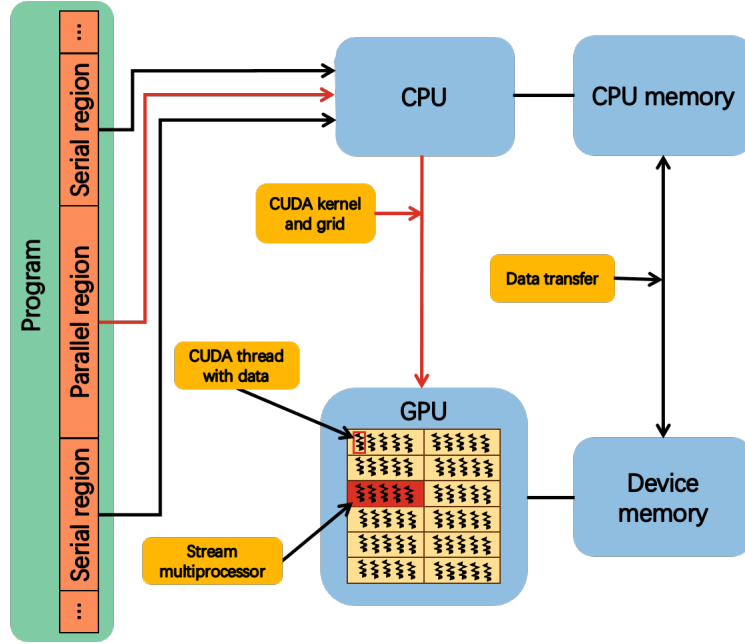


Figure 2: Framework of CUDA with GPU.

3.2. CUDA implementation

With the connectivities above, the cell-level parallelism will be implemented with single GPU and Compute unified device architecture (CUDA). CUDA is a parallel computing platform developed by NVIDIA for general-purpose computing with GPU. It provides the parallel computing architecture that introduces a novel programming model established on high abstraction levels. From the perspective of CUDA, GPU is viewed as a computer device capable of executing thousands of threads simultaneously and it works as a co-processor to the main CPU. The brief framework of such process is shown in Figure.2. The CPU is regarded as host, and GPU is treated as device. Data-parallel, compute-intensive operations running on the host are transferred to device by using kernels, and kernels are executed on the device by many different threads. For CUDA, these threads are organized into thread blocks, and thread blocks constitute a grid. Such computational structures build connection with Nvidia GPU hardware architecture. The Nvidia GPU consists of multiple streaming multiprocessors (SMs), and each SM contains streaming processors (SPs). When invoking a kernel, the blocks of grid are distributed to SMs, and the threads of each block are executed by SPs. The key of parallel computation using CUDA and single GPU is setting kernels and corresponding grids.

For the explicit computation, HGKS on unstructured meshes is fully parallelized, and the main process of HGKS code is introduced in Algorithm.2. Except for the data transfer involved in "Load unstructured meshes information" and "Export of output files", the rest parts are parallel regions and can be set as kernels. To achieve the cell-level parallelism of the algorithm, the configuration of grids requires the equivalence of the number of threads and number of cells. The indices of threads should be mapped one-to-one with the indices

Algorithm 2 HGKS on unstructured meshes

```
Load unstructured meshes information
Establish geometric connectivity in data structure
Build two-layer neighbors with boundary conditions
while Time  $\leq$  StopTime do
  Calculate time step
  for Step = 1 to 2 do
    WENO reconstruction
    Compute flux
    Update flow variables
  end for
  if Time == OutputTime then
    Export of output files
  end if
end while
```

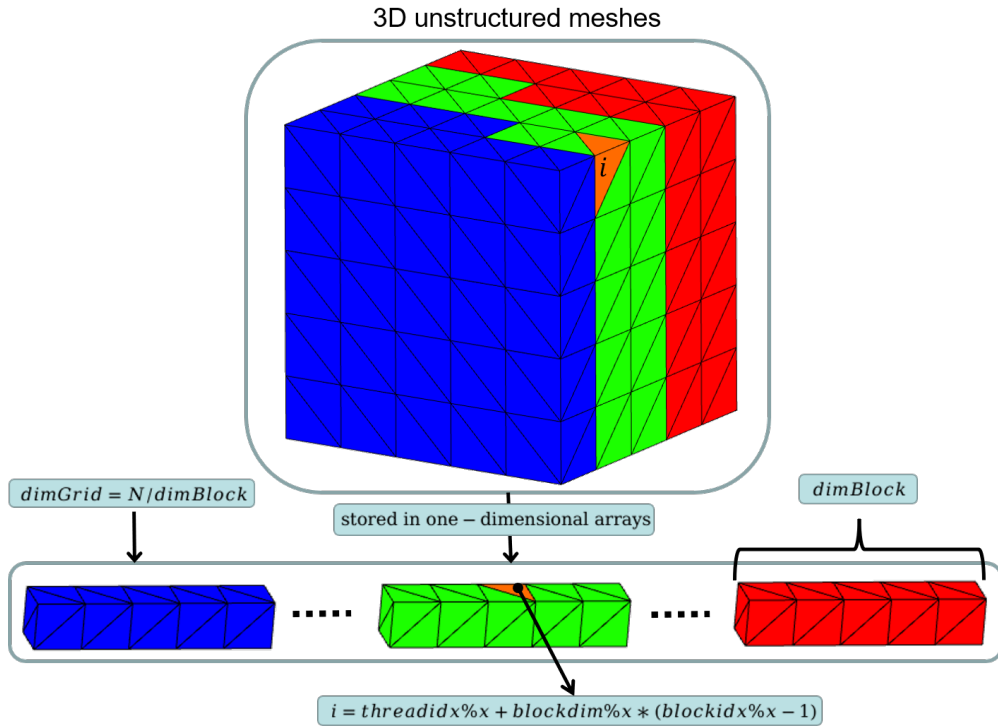


Figure 3: Process of setting grid for unstructured meshes.

of cells. The kernel invocation can be described as

$$kernel \lll dimGrid, dimBlock \ggg,$$

where $dimGrid$ and $dimBlock$ are either integer expressions (for one-dimensional grids and

thread blocks), or integer arrays (for two-dimensional or three-dimensional grids and thread blocks). $dimGrid$ describes the number of thread blocks in the grid, and the number of threads in each thread block can be determined by $dimBlock$. The brief process of setting grids is shown in Figure.3. For unstructured meshes, the indices of cells are provided by a one-dimensional array, and $dimGrid$ and $dimBlock$ will be set as two integers. A single thread block, which contains the same number of threads as the cells, should be used in the grid. However, there are some limitations on the number of threads in each thread block, i.e., each thread block contains a maximum of 1024 threads. Assume the total number of cells is N , $dimGrid$ is defined as $dimGrid = N/dimBlock$. If N is not divisible by $dimBlock$, an extra thread block is needed. The relationship between the cells indices i and threads indices can be defined as

$$i = threadidx \% x + blockdim \% x * (blockidx \% x - 1).$$

Thus, HGKS code can be implemented with specifying kernels and grids with single GPU.

4. Multiple-GPU implementation

For the HGKS code on structured meshes [23], the one-dimensional decomposition is adopted, and MPI processes are created to manage GPU computation and data transfer. The number of parts equals to the number of GPUs. Each GPU inherits the configuration of single GPU implementation to complete parallel computation. In this paper, such framework will be extended to HGKS on unstructured meshes. The implementation is presented in this section, including domain decomposition and the combination of MPI and CUDA.



Figure 4: Pre-processing of generating geometric information for each subdomain.

4.1. Domain decomposition

METIS library [12] is used for the domain decomposition of unstructured meshes in a reasonable way. For the load balance of computation, the number of meshes assigned to each device is nearly identical. For the efficiency of data communication, the number of adjacent subdomain belong to different devices is minimized. METIS only provides the indices of cells for each subdomain, and the geometric connectivity are broken after domain decomposition. The pre-processes for data localization and independence are shown in Figure.4.

According to the cell information provided by METIS and the geometric connectivities of the whole domain, the nodes and faces can be classified into the corresponding subdomain. Duplicate nodes and faces are included in different subdomains as well. A new set of indices for nodes, faces, and cells is formed for each subdomain after decomposition. There

are two indices for nodes, faces and cells, i.e., the old rank in the domain and the new rank in the subdomains. The mappings of these indices are built by two-dimensional arrays, i.e. *SNodeToTNode* and *TNodeToSNode*. *SNodeToTNode*[i][j] provides the index of node i of subdomain j in the domain, and *TNodeToSNode*[i][j] offers the index of node i of the domain in subdomain j . The mappings of the indices of faces and cells are established similarly. The connectivities of the domain can be converted to the connectivities of each subdomain by using these mappings, and the cell-to-face, face-to-node and cell-to-node connectivities for each subdomain are also obtained. Due to large stencil for WENO reconstruction, the data exchange becomes more complicated. As shown in Figure.5, some neighboring cells of each subdomain are located in other subdomains. To compute the fluxes of inner boundary faces, the geometric information of the two cells sharing the inner boundary face and their two-layer neighbors must be provided, which means three-layer neighbors for the inner boundary should be accessed. These three-layer neighbors are added to subdomains as ghost cells in the pre-processing. According to the cell-to-neighbor connectivity, these three-layer neighbors can be found, and their indices will be added to the mappings between the domain and subdomains. The indices of their nodes and faces will be added to subdomains in the same way. Except for geometric information, the conservative variables stored in three-layer neighbors should be transferred to ghost cells after the update of flow variables. The indices of these neighbors are used to build mappings between two subdomains for MPI communication. These mappings are stored in two-dimensional array, i.e., *CellSend*. *CellSend*[i][2] provides the index of cell i in the subdomain and the target subdomain. Through such mappings, the conservative variables on the ghost cells can be updated accurately. With the pre-processing above, the data localization and independence of each subdomain are maintained.

4.2. Combination of MPI and CUDA

MPI is a standard parallelization library adopted on distributed memory platforms. It is widely used in CFD to meet the demands of large-scale computations. The idea of creating MPI processes for one-to-one GPU management and communication is maintained. The framework of multiple-GPU implementation with CUDA and MPI is shown in Figure.6. MPI is based on Single Program Multiple Data (SPMD) model, in which a single program is executed simultaneously with multiple data. For HGKS code with CUDA and MPI, the copy of program and data of each subdomain are distributed to each MPI process. The CUDA code for single GPU can be inherited as a main part of multiple-GPU implementation, and the rest part for multiple-GPU implementation is MPI communication. Typically, a multi-GPU cluster consists of multiple nodes and each node contains the same number of GPUs and CPUs. The CUDA-Aware MPI library[14] is used in this study. It is an MPI implementation that enables direct communication with GPU memory. This capability markedly enhances parallel computing efficiency in multi-GPU environments. NVLink and GPU Direct Remote Direct Memory Access (RDMA) are used to support direct GPU memory transfer within nodes and across nodes, which improves communication efficiency among GPUs.

In the previous study, as shown in Figure.7, the blocking communication is employed in a staggered manner for the HGKS code on structured meshes [23]. Each subdomain

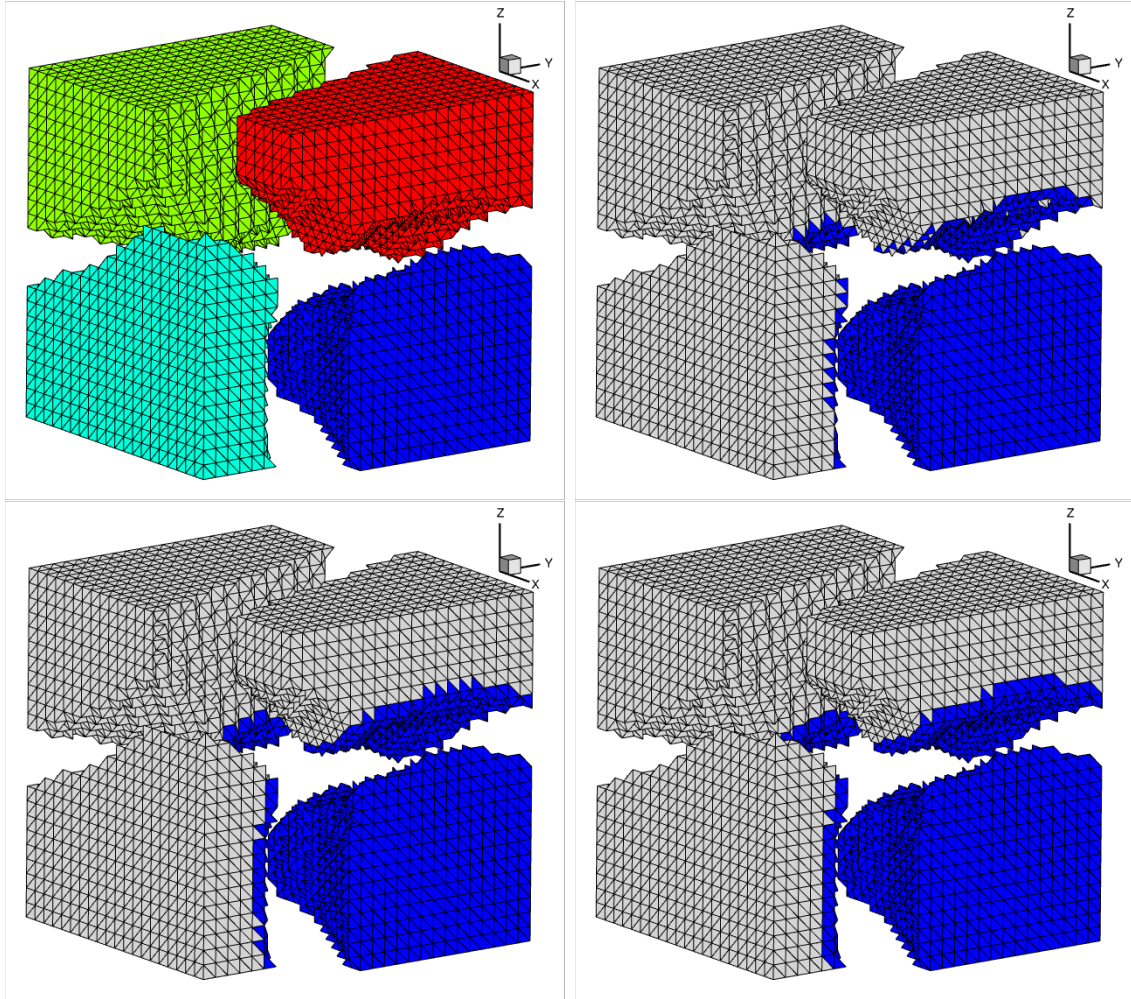


Figure 5: Unstructured meshes are split by METIS and three-layer neighbors of subdomain in Blue distributed in other subdomains.

only need to transfer data with two neighboring subdomains, and the communications in purple has to wait for the communications in green. All other computations have to wait for the communication, even though some computations do not require the data from the communication. For the HGKS code on unstructured meshes, the conservative variables of neighboring cells located in other subdomains should be transferred to the target subdomain for WENO reconstruction. Each subdomain has to communicate with all other subdomains for the unstructured meshes. If the strategy for structured mesh is extended to unstructured mesh, a significant amount of time will be spent for communication, and a new strategy for communication must be proposed. Non-blocking communication is chosen for HGKS on unstructured meshes, and the brief setting of communication is shown in Figure.8. Non-blocking communication `MPI_SEND/IRECV` allows processes to initiate communication operations and then proceed with other computations. GPU i can transfer data of three-layer neighbors with other GPUs by using `MPI_SEND/IRECV`, simultane-

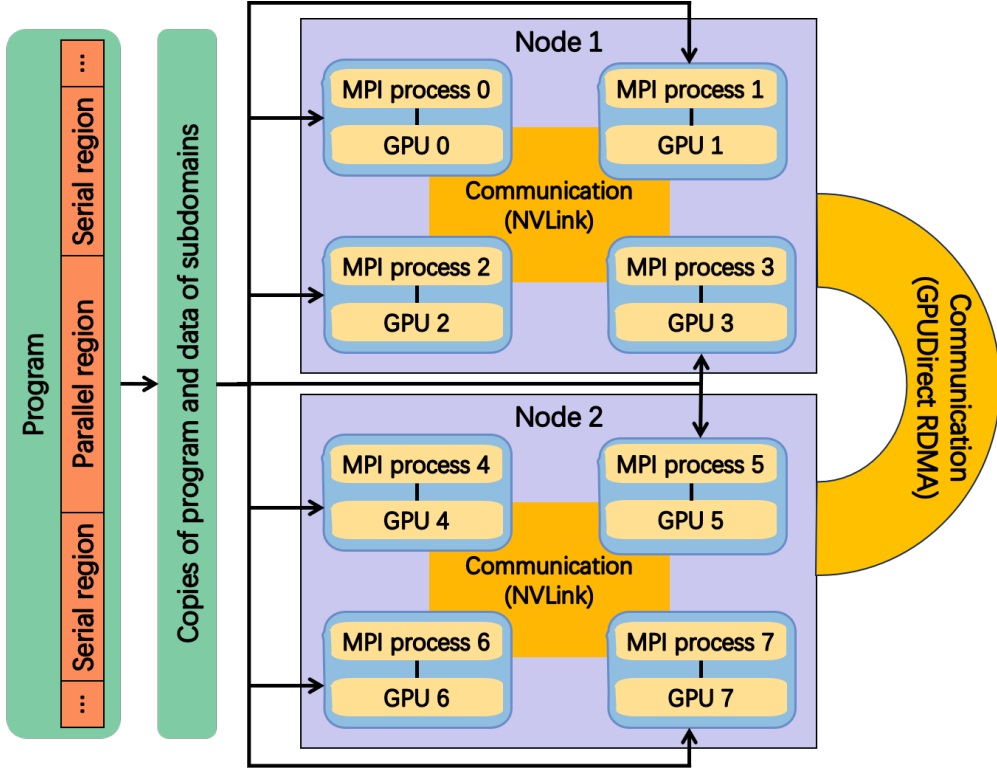


Figure 6: Framework of multi-GPU with CUDA and MPI.

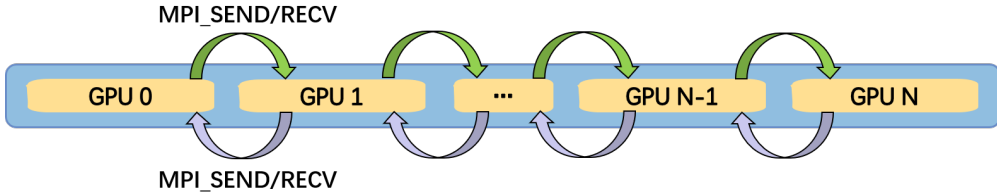


Figure 7: Staggered blocking communication for case of structured meshes.

ously. The computations that do not require these data can be executed on GPU during communication. Before WENO reconstruction, `MPI_WAITALL` is called to ensure that all communication about GPU i has been completed. `MPI_ALLREDUCE` and `MPI_BARRIER` are used to deal with the operation of global unification. The indices of cells are discontinuous, and the data packaging is added as a new computational task in the program. By using the frame described above, HGKS on unstructured meshes can be computed in parallel on GPUs.

5. Numerical tests

In this section, the numerical examples will be presented to validate the performance of GPU code by the accuracy test and the flows passing through a sphere. For the GPU

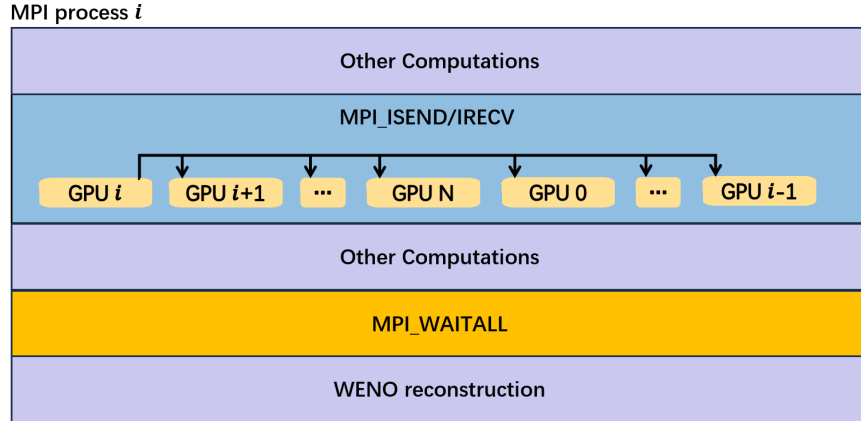


Figure 8: Non-blocking communication for case of structured meshes.

computations, the Nvidia RTX A5000 GPU and Nvidia Tesla V100 GPU are used with Nvidia CUDA and CUDA-Aware MPI of NVIDIA HPC SDK 21.7. As reference, the CPU codes run on the station with 2 Intel(R) Xeon(R) Gold 5120 CPU using OpenMP directives. The detailed parameters of CPU and GPU are given in Table.1 and Table.2, respectively. For RTX A5000 GPU, the GPU-GPU communication is achieved by connection traversing PCIe, and there are 2 RTX A5000 GPUs in one node. For Tesla V100 GPU, there are 8 GPUs inside one GPU node, and more nodes are needed for more than 8 GPUs. The GPU-GPU communication in one GPU node is achieved by Nvidia NVLink. The communication across GPU nodes can be achieved by GPU Direct RDMA via iWARP, RDMA over Converged Ethernet (RoCE) or InfiniBand. In this paper, RoCE is used for communication across GPU nodes.

	CPU	Clock rate	Memory size
Station (56 cores)	Intel(R) Xeon(R) Gold 5120 CPU	2.20 GHz	768 GB

Table 1: The detailed parameters of CPU.

	Nvidia RTX A5000	Nvidia Tesla V100
Clock rate	1.17 GHz	1.53 GHz
Stream multiprocessor	64	80
FP32 precision performance	27.77 Tflops	15.7 Tflops
FP64 precision performance	867.8 Gflops	7834 Gflops
GPU memory size	24 GB	32 GB
Memory bandwidth	768 GB/s	897 GB/s

Table 2: The detailed parameters of GPU.

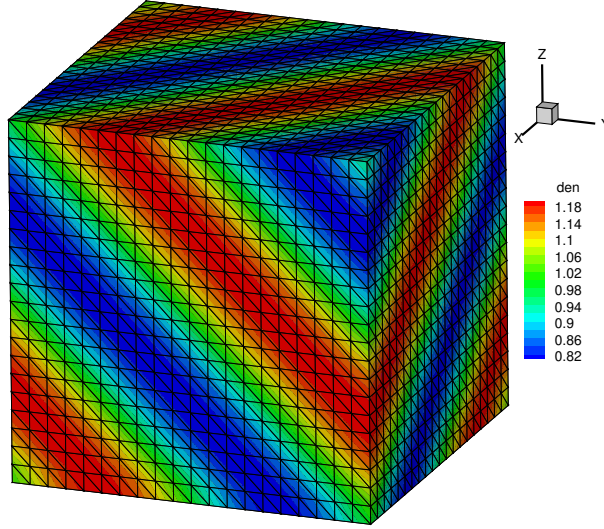


Figure 9: Accuracy test: the computational mesh with $20^3 \times 6$ cells and the density distribution at $t = 2$.

5.1. Accuracy test

In this case, the three-dimensional advection of density perturbation is used to test the order of accuracy with the tetrahedron meshes. For this case, the computational domain is $[0, 2] \times [0, 2] \times [0, 2]$ and the initial condition is given as follows

$$\begin{aligned}\rho_0(x, y, z) &= 1 + 0.2 \sin(\pi(x + y + z)), & p_0(x, y, z) &= 1, \\ U_0(x, y, z) &= 1, & V_0(x, y, z) &= 1, & W_0(x, y, z) &= 1.\end{aligned}$$

The periodic boundary condition is applied on all boundaries, and the exact solution is

$$\begin{aligned}\rho(x, y, z, t) &= 1 + 0.2 \sin(\pi(x + y + z - t)), & p(x, y, z, t) &= 1, \\ U(x, y, z, t) &= 1, & V(x, y, z, t) &= 1, & W(x, y, z, t) &= 1.\end{aligned}$$

In smooth flow regions, $\tau = 0$ and the gas-distribution function reduces to

$$f(\mathbf{x}_G, t, \mathbf{u}, \xi) = g(1 + At).$$

For this case, a series of meshes with $6 \times N^3$ tetrahedron cells are used, where every cubic is divided into six tetrahedron cells. The computational mesh with $20^3 \times 6$ cells are shown in Figure. 9. The density distribution at $t = 2$ is also shown in Figure. 9, and the L^1 and L^2 errors and orders of accuracy at $t = 2$ are presented in Tab.3, where the expected order of accuracy is achieved.

To test the performance of single-GPU code, this case is run with both Nvidia RTX A5000 and Nvidia Tesla V100 GPUs using Nvidia CUDA. As a comparison, the CPU code running on the Intel Xeon(R) Gold 5120 CPU is also tested. The execution times with different meshes are shown in Table.4, where the total execution time for CPU and GPUs

mesh	L^1 error	Order	L^2 error	Order
$10^3 \times 6$	6.6070E-02		2.5938E-02	
$20^3 \times 6$	8.7117E-03	2.9230	3.4159E-03	2.9247
$40^3 \times 6$	1.0994E-03	2.9862	4.3094E-04	2.9867
$80^3 \times 6$	1.3768E-04	2.9973	5.3968E-05	2.9973
$160^3 \times 6$	1.7252E-05	2.9965	6.7761E-06	2.9936

Table 3: Accuracy tests: errors and orders of accuracy with tetrahedron meshes.

Mesh size	Station	RTX A5000	Speedup	Tesla V100	Speedup
6×10^3	5.44	1.05	5.18	0.55	9.89
6×20^3	58.12	10.1	5.75	5.99	9.70
6×40^3	840.89	150.57	5.58	86.01	9.78
6×80^3	12821.05	2342.37	5.47	1333.33	9.62

Table 4: Accuracy tests: The detailed computational times(s) and speedup for RTX A5000, and 56-core station CPU with OpenMP is used as reference.

No. GPUs	6×40^3	Parallel efficiency
1	86.01	
2	44.26	0.97
4	23.79	0.90
8	13.73	0.78
No. GPUs	6×80^3	Parallel efficiency
1	1333.33	
2	672.23	0.99
4	343.87	0.97
8	180.19	0.92
No. GPUs	6×160^3	Parallel efficiency
4	5375.23	
8	2710.12	0.99

Table 5: Accuracy tests: The detailed computational time(s) and parallel efficiency for Tesla V100.

are given at $t = 2$. Due to the limitation of single GPU memory size, the tetrahedron meshes from 6×10^3 to 6×80^3 cells are used. For the CPU computation, 56 cores are utilized with OpenMP parallel computation, and the corresponding execution time is used as the base

for following comparisons. The speedups are given in Table.4, which is defined as

$$\text{Speedup} = \frac{\text{CPU time}}{\text{GPU time}}.$$

Compared with the CPU code using 56 cores, $\approx 5x$ speedup is achieved by single RTX A5000 GPU, and $\approx 9x$ speedup is achieved by single Tesla V100 GPU. Even though the Tesla V100 is approximately 15 times faster than the RTX A5000 in FP64 precision computation ability, Tesla V100 only performs 2 times faster than RTX A5000. Due to the limitation of single-GPU, the multiple-GPU accelerated HGKS code has to be implemented. To further show the performance of GPU computation, the scalability is defined as

$$\text{Parallel efficiency} = \frac{\text{single-GPU time}}{\text{multiple-GPU time} \times \text{number of GPUs}}.$$

The detailed data for Tesla V100 GPU are given in Table.5, in which 1 to 8 GPUs are used for the case with 6×40^3 and 6×80^3 cells, and 4 to 8 GPUs are used for the case with 6×160^3 cells. For the ideal parallel computations, the parallel efficiency would be equal to 1 with the increase of GPUs. However, such parallel efficiency is not possible due to the communication delay among the computational cores and the idle time of computational nodes associated with load balancing. As shown in Table.5, the explicit formulation of HGKS scales properly with the increasing number of GPU. Each GPU in multiple-GPU implementation can achieve more than 97% of the efficiency of single-GPU implementation with suitable computational work-load.

In this case, the GPU-accelerated HGKS is compiled with both FP32 precision and FP64 precision. For most GPUs, the performance of FP32 precision is stronger than FP64 precision. Because of the reduction in device memory and improvement of arithmetic capabilities on GPUs, the benefits can be achieved by using FP32 precision compared to FP64 precision. In view of these strength, FP32-based and mixed-precision-based high-performance computing start to be explored [15, 10]. The comparison study with FP32 and FP64 precision for the direct numerical simulation is provided in our previous work [23]. For the HGKS code on unstructured mesh, such comparison is also given. For simplicity, the memory cost and computational time for the accuracy test are provided in Table.6, where the execution times are given in terms of second and the memory cost is in MiB. As expected, the memory of FP32 precision is about half of that of FP64 precision for both RTX A5000 and Tesla V100 GPUs. Compared with FP64-based simulation, 4.6x speedup is achieved for RTX A5000 GPU and 2.6x speedup is achieved for Tesla V100 GPU. The errors and orders of accuracy with tetrahedron cells using RTX A5000 and FP32 precision is given in Table.7, which deviates with the error in Table.4 slightly. In terms of the problems without very strict requirements in accuracy, such as the third-order scheme on unstructured meshes, FP32 precision may be used due to its improvement of efficiency and reduction of memory. However, for the direct numerical simulation of turbulences, the numerical results indicate that FP32 precision is not enough [23]. It strongly suggests that the FP64 precision performance of GPU still requires to be improved to accommodate the increasing requirements of

RTX A5000	Computation time with FP32	Computation time with FP64	Ratio
6×40^3	32.53	150.57	4.63
6×80^3	521.91	2342.37	4.49
RTX A5000	Memory cost with FP32	Memory cost with FP64	Ratio
6×40^3	1470	2578	1.75
6×80^3	7762	14822	1.91
Tesla V100	Computation time with FP32	Computation time with FP64	Ratio
6×40^3	32.78	86.01	2.62
6×80^3	490.64	1333.33	2.72
Tesla V100	Memory cost with FP32	Memory cost with FP64	Ratio
6×40^3	1843	3157	1.71
6×80^3	8095	14993	1.85

Table 6: Accuracy test: the comparison of computational time (s) and memory (MiB) for FP32 and FP64 precision with single RTX A5000 and Tesla V100.

mesh	L^1 error	Order	L^2 error	Order
6×10^3	6.6074E-02		2.5940E-02	
6×20^3	8.7154E-03	2.9225	3.4173E-03	2.9242
6×40^3	1.1019E-03	2.9835	4.3188E-04	2.9842
6×80^3	1.4119E-04	2.9644	5.5303E-05	2.9652

Table 7: Accuracy test: errors and orders of accuracy with tetrahedron cells using RTX A5000 and FP32 precision.

GPU-based HPC.

5.2. Flows passing through a sphere

This case is used to test the capability in resolving from the low-speed to transsonic flows, and the initial condition is given as a free stream condition

$$(\rho, U, V, W, p)_\infty = (1, Ma_\infty, 0, 0, 1/\gamma),$$

where $\gamma = 1.4$, Ma_∞ is the Mach number of free stream, and the diameter of the sphere is $D = 1$. As shown in Figure.10, this case is performed by the hexahedral meshes. These meshes are composed with six parts and each part contains $N \times N \times 2N$ cells, and the total number of cell is $12 \times N^3$. The subsonic case with $Re = 118$ and $Ma_\infty = 0.2535$ and the transsonic case with $Re = 300$ and $Ma_\infty = 1.5$ are tested. The inlet and outlet boundary conditions are given according to Riemann invariants, and the non-slip adiabatic boundary condition is imposed for viscous flows on the surface of sphere. The dynamic viscosity is

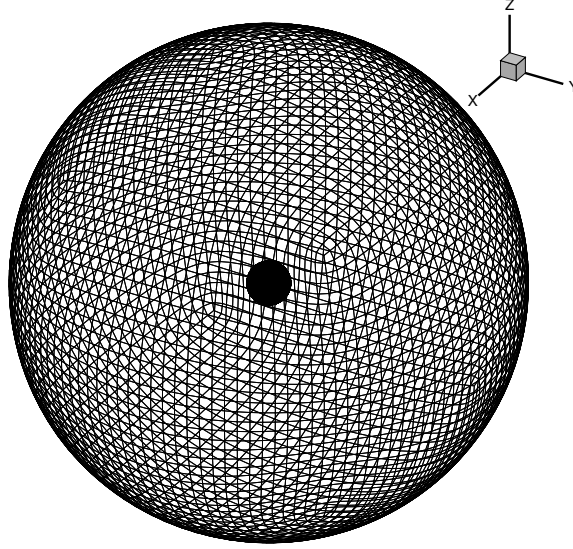


Figure 10: Flows passing through a sphere: the mesh distribution with $6 \times 16 \times 16 \times 32$ cells.

given by

$$\mu = \mu_{\infty} \left(\frac{T}{T_{\infty}} \right)^{0.7},$$

where T_{∞} and μ_{∞} are free stream temperature and viscosity. The density, velocity and streamline distributions at vertical centerline planes are shown in Figure.11 for the subsonic case and transsonic case using 12×64^3 cells. The quantitative results of separation angle θ and closed wake length L are given in Table.8 and Table.9, respectively. The current scheme gives a better values of L and θ , which are closer to the experiment data. The performance would be better with a refined mesh. Quantitative results agree well with the benchmark solutions [?], and the slight deviation of compact gas-kinetic scheme [11] might caused by the coarser mesh.

To show the performance with multiple GPUs, this case is tested by the meshes from 12×16^3 to 12×128^3 cells. For the mesh with 12×16^3 and 12×32^3 cells, the maximum of GPU is 8, and NVLink are used within node. For the mesh with 12×64^3 and 12×128^3 cells, the maximum number of GPU is 16. NVLink and RDMA via RoCE are used within node and across nodes respectively. The log-log plot for n and total time are shown in Figure.12. Conceptually, the total computation amount increases with a factor of 16, when the number of N doubles. With the log-log plot for n and total time, an ideal scalability would follow -1 slope. However, it's not possible to have ideal scalability because of communication delays and idle times. As expected, the explicit formulation of HGKS scales properly with the increasing number of GPUs. When GPU code using more than 8 GPUs, the communication across GPU nodes with RoCE is required, which accounts for the worse scalability using 16

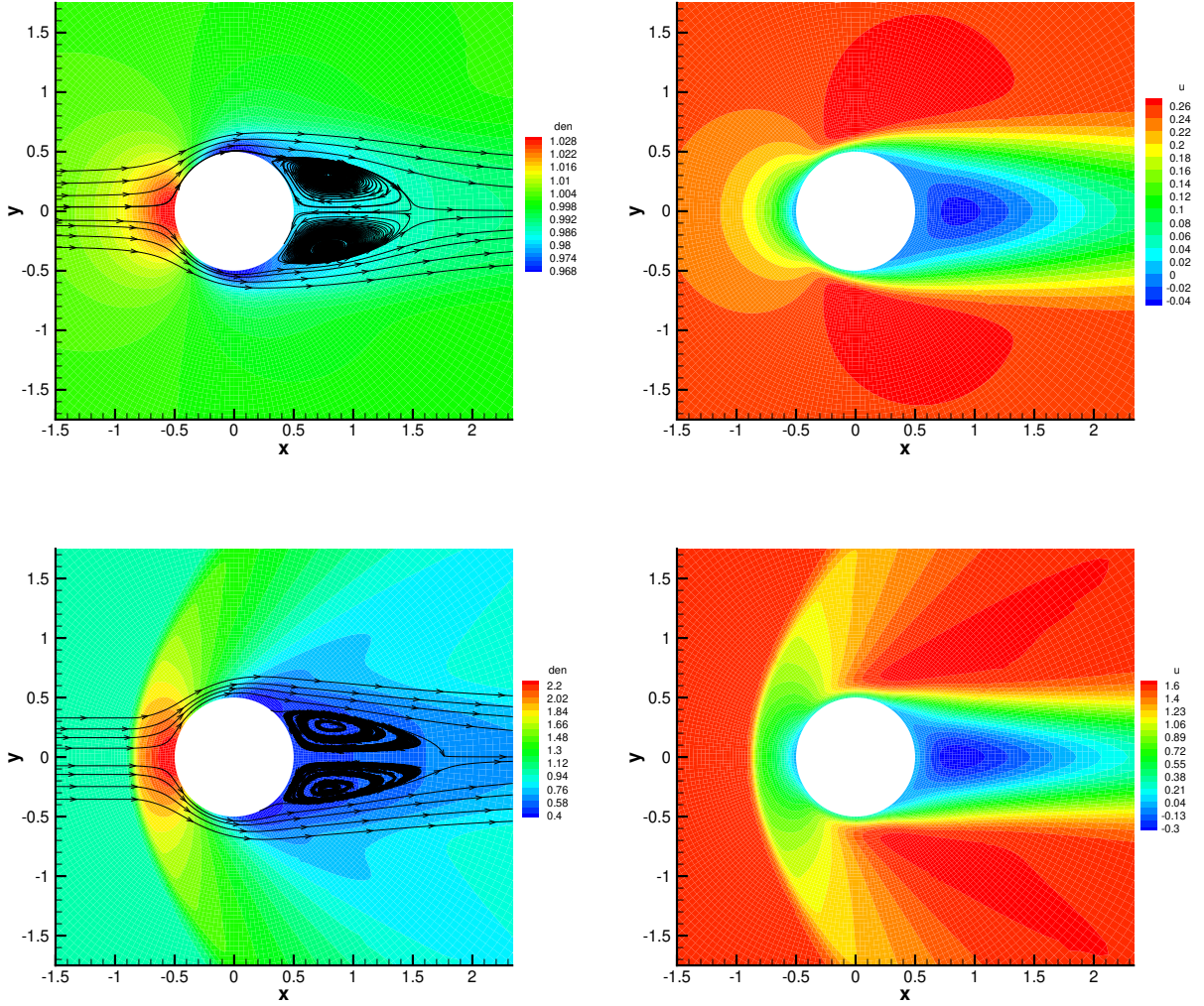


Figure 11: Flows passing through a sphere: the density, streamline and mach distribution for the case with $Re = 118$ and $Ma_\infty = 0.2535$ (top) and $Re = 300$ and $Ma_\infty = 1.5$ (bottom) using 12×64^3 cells.

GPUs.

Meanwhile, the detailed data for Tesla V100 GPU are given in Table.5, in which total computational time and the percentage of the time for communication are given. Specifically, the communication time is consist of the time for MPI_SEND and MPI_RECV for the transfer of conservative variables of ghost cells, MPI_WAITALL for ensuring completion of communications, and MPI_ALLREDUCE for global time step. The communication across GPU nodes with RoCE consumes longer time than the communication in single GPU node with NVLink. The performance of communication across GPU nodes with InfiniBand will be tested, which is designed for HPC centers to improve efficiency among GPU nodes.

Scheme	Computational Mesh	L	θ
Current result	3145728 cells, Hex	0.99	128.4
LUSGS GKS [28]	190464 cells, Hex	0.91	124.5
GMRES GKS [28]	190464 cells, Hex	0.91	124.5
GMRES DDG [4]	1608680 cells, Hybrid	0.96	123.7
Experiment [21]	-	1.07	151.0

Table 8: Flows passing through a sphere: the quantitative comparisons of closed wake length L and separation angle θ for $Re = 118$ and $Ma_\infty = 0.2535$.

scheme	Computational Mesh	L	θ
Current result	3145728 cells, Hex	1.18	136.8
LUSGS GKS [28]	190464 cells, Hex	1.17	135.1
GMRES GKS [28]	190464 cells, Hex	1.17	135.4

Table 9: Flows passing through a sphere: the quantitative comparisons of closed wake length L and separation angle θ for $Re = 300$ and $Ma_\infty = 1.5$.

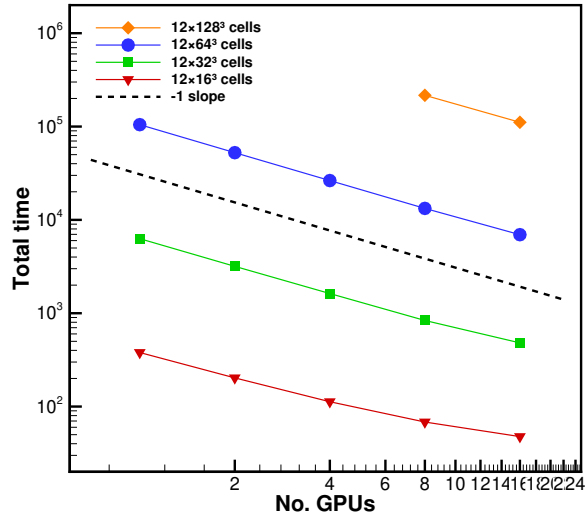


Figure 12: Flows passing through a sphere: the speedup of Tesla V100 GPUs with 12×16^3 to 12×128^3 cells.

6. Conclusion

In this paper, to accelerate the computation, HGKS is implemented with GPU using CUDA on unstructured meshes. For single-GPU computation, the connectivity of geomet-

No. GPUs ($N = 16$)	Total	Communication (%)
1	0.105	
2	0.056	0.426
4	0.031	0.823
8	0.019	1.648
No. GPUs ($N = 32$)	Total	Communication (%)
1	1.747	
2	0.883	0.024
4	0.452	0.115
8	0.232	0.554
No. GPUs ($N = 64$)	Total	Communication (%)
1	29.096	
2	14.587	0.034
4	7.331	0.082
8	3.688	0.149
16	1.929	3.169
No. GPUs ($N = 128$)	Total	Communication (%)
8	60.058	0.063
16	30.876	2.183

Table 10: Flows passing through a sphere: the detailed computational time (h) and parallel efficiency for Tesla V100.

ric information is generated for the requirement of data localization and independence. A simple setting for thread and block is adopted for arbitrary unstructured meshes, and the executions are implemented automatically by GPU. To further improve the computational efficiency and enlarge the computational scale, the HGKS code is also implemented with multiple GPUs using MPI and CUDA. For multiple-GPU computation, the domain decomposition and data exchange need to be taken into account. The domain is decomposed into subdomains by METIS, and the MPI processes are created for the control of each process and communication among GPUs. With reconstruction of connectivity and adding ghost cells, the main configuration of CUDA for single-GPU can be inherited by each GPU. For single-GPU implementation using CUDA, compared with the CPU code using 2 Intel(R) Xeon(R) Gold 5120 CPUs with OpenMP directives, 5x speedup is achieved for RTX A5000 and 9x speedup is achieved for Tesla V100. For multiple-GPU with CUDA and MPI, the HGKS is strongly scalable with the increasing number of GPUs. Nearly linear speedup can be achieved under suitable computational work-load. Numerical performance shows that the data communication crossing GPUs through MPI costs the relative little time. The comparisons between FP32 (single) precision and FP64 (double) precision of GPU are also given. The accuracy test is used for evaluate the effect of precision on computation of HGKS. As expected, the efficiency can be improved and the memory cost can be reduced with FP32

precision. Compared with the results of FP64 precision, the errors of the accuracy increase slightly and the third-order can be maintained.

Acknowledgements

The current research of L. Pan is supported by Beijing Natural Science Foundation (1232012), National Natural Science Foundation of China (11701038) and the Fundamental Research Funds for the Central Universities.

Declaration of competing interest

The authors declare that they have no known competing financial interests or personal relationships that could have appeared to influence the work reported in this paper.

Data availability

The data that support the findings of this study are available from the corresponding author upon reasonable request.

References

- [1] P.L. Bhatnagar, E.P. Gross, M. Krook, A Model for Collision Processes in Gases I: Small Amplitude Processes in Charged and Neutral One-Component Systems, *Phys. Rev.* 94 (1954) 511-525.
- [2] G.Y. Cao, L. Pan, K. Xu, High-order gas-kinetic scheme with parallel computation for direct numerical simulation of turbulent flows, *J. Comput. Phys.* 448 (2022) 110739.
- [3] S. Chapman, T.G. Cowling, *The Mathematical theory of Non-Uniform Gases*, third edition, Cambridge University Press (1990).
- [4] J. Cheng, X. Liu, T.G. Liu, H. Luo, A. Parallel, High-order direct discontinuous Galerkin method for the Navier-Stokes equations on 3D hybrid grids, *Commun. Comput. Phys.* 21 (2017) 1231-1257.
- [5] G.L. Dang, S.W. Liu, T.B. Guo, J.Y. Duan, X.L. Li, Direct numerical simulation of compressible turbulence accelerated by graphics processing unit: An open-source high accuracy accelerated computational fluid dynamic software, *Phys. Fluids* 34 (2022) 126106.
- [6] V. Delmas, A. Soullaimani, Multi-GPU implementation of a time-explicit finite volume solver using CUDA and a CUDA-Aware version of OpenMPI with application to shallow water flows, *Comput. Phys. Commun.* 271 (2022) 108190.
- [7] M. C. Esposito, N. Scapin, A.D. Demou, M.E. Rosti, P. Costa, F. Spiga, L. Brandt, FluTAS: A GPU-accelerated finite difference code for multiphase flows, *Comput. Phys. Commun.* 284 (2023) 108602.
- [8] G.C. Fan, W.W. Zhao, S.B. Yao, Z.Z. Jiang, W.F. Chen, The implementation of the three-dimensional unified gas kinetic wave-particle method on multiple graphics processing units, *Phys. Fluids* 35 (2023) 086108.
- [9] M.P.I. Forum, *MPI: A Message-Passing Interface Standard, Version 2.2*. High Performance Computing Center Stuttgart (2009).
- [10] A. Haidar, H. Bayraktar, S. Tomov, J. Dongarra, N.J. Higham, Mixed-precision iterative refinement using tensor cores on GPUs to accelerate solution of linear systems, *Proc. R. Soc. A.* (2020) 476: 20200110.
- [11] X. Ji, L. Pan, W. Shyy, K. Xu, A compact fourth-order gas-kinetic scheme for the Euler and Navier–Stokes equations, *J. Comput. Phys.* 372 (2018) 446-472

- [12] G. Karypis, V. Kumar, METIS: a software package for partitioning unstructured graphs, partitioning meshes, and computing fill-reducing orderings of sparse matrices version 5.1.0 (2013) <http://www.cs.umn.edu/karypis>.
- [13] K. Karzhaubayev, L.P. Wang, D. Zhakebayev, DUGKS-GPU: An efficient parallel GPU code for 3D turbulent flow simulations using Discrete Unified Gas Kinetic Scheme, *Comput. Phys. Commun.* 301 (2024) 109216.
- [14] J. Kraus, An Introduction to CUDA-Aware MPI. <https://developer.nvidia.com/blog/introduction-cuda-aware-mpi/> (2013).
- [15] M. Lehmann, M.J. Krause, G. Amati, M. Sega, J. Harting, S. Gekle, On the accuracy and performance of the lattice Boltzmann method with 64-bit, 32-bit and novel 16-bit number formats, *Phys. Rev. E* 106 (2022) 015308.
- [16] J.Q. Li, Z.F. Du, A two-stage fourth order time-accurate discretization for Lax-Wendroff type flow solvers I. hyperbolic conservation laws, *SIAM J. Sci. Computing*, 38 (2016) 3046-3069.
- [17] J.Q. Li, Two-stage fourth order: temporal-spatial coupling in computational fluid dynamics (CFD), *Advances in Aerodynamics* (2019) 1:3.
- [18] J. O’Connor, J.M. Dominguez, B.D. Rogers, S.J. Lind, P.K. Stansby, Eulerian incompressible smoothed particle hydrodynamics on multiple GPUs, *Comput. Phys. Commun.* 273 (2022) 108263.
- [19] L. Pan, K. Xu, Q.B. Li, J.Q. Li, An efficient and accurate two-stage fourth-order gas-kinetic scheme for the Navier-Stokes equations, *J. Comput. Phys.* 326 (2016) 197-221.
- [20] S. Pirozzoli, J. Romero, M. Fatica, R. Verzicco, P. Orlandi, One-point statistics for turbulent pipe flow up to $Re_\tau \approx 6000$, *J. Fluid. Mech.* 926 (2021) A28.
- [21] S. Taneda, Studies on wake vertices, experimental investigation of the wake behind a sphere at low Reynolds numbers, *J. Phys. Soc. Jpn.* 11 (1956) 1104-1108.
- [22] Y.H. Wang, L. Pan, Three-dimensional discontinuous Galerkin based high-order gas-kinetic scheme and GPU implementation, *Computers and Fluids* 242 (2022) 105510.
- [23] Y.H. Wang, G.Y. Cao, L. Pan, Multiple-GPU accelerated high-order gas-kinetic scheme for direct numerical simulation of compressible turbulence, *J. Comput. Phys.* 448 476 (2023) 111899.
- [24] C.F. Xu, X.G. Deng, et al., Collaborating CPU and GPU for large-scale high-order CFD simulations with complex grids on the TianHe-1A supercomputer, *J. Comput. Phys.* 278 (2014) 275-297.
- [25] K. Xu, A gas-kinetic BGK scheme for the Navier-Stokes equations and its connection with artificial dissipation and Godunov method, *J. Comput. Phys.* 171 (2001) 289-335.
- [26] K. Xu, *Direct modeling for computational fluid dynamics: construction and application of unified gas kinetic schemes*, World Scientific (2015).
- [27] Y.Q. Yang, L. Pan, K. Xu, Three-dimensional third-order gas-kinetic scheme on hybrid unstructured meshes for Euler and Navier-Stokes equations, *Comput. Fluids* 255 (2023) 105834.
- [28] Y.Q. Yang, L. Pan, K. Xu, Implicit high-order gas-kinetic schemes for compressible flows on three-dimensional unstructured meshes I: Steady flows, *J. Comput. Phys.* 505 (2024) 112902
- [29] P. K. Yeung, K. Ravikumar, Advancing understanding of turbulence through extreme-scale computation: Intermittency and simulations at large problem sizes, *Phys. Rev. Fluids* 5 (2020) 110517.
- [30] J. Zhu, J.X. Qiu, A new fifth order finite difference WENO scheme for solving hyperbolic conservation laws, *J. Comput. Phys.* 318 (2016) 110-121.
- [31] J. Zhu, J.X. Qiu, New finite volume weighted essentially non-oscillatory scheme on triangular meshes, *SIAM J. Sci. Computing* 40 (2018) 903-928.